Received: 8 March 2023 | Revised: 2 May 2023 | Accepted: 29 May 2023

DOI: 10.1002/inf2.12462

RESEARCH ARTICLE

WILEY

Beneficial impact of lithium bis(oxalato)borate as electrolyte additive for high-voltage nickel-rich lithium-battery cathodes

Fanglin Wu[1,2] | **Angelo Mullaliu**[1,2,3] | **Thomas Diemant**[1,2] | **Dominik Stepien**[1,2] | **Tatjana N. Parac-Vogt**[3] | **Jae-Kwang Kim**[4] | **Dominic Bresser**[1,2] | **Guk-Tae Kim**[1,2,4] | **Stefano Passerini**[1,2,5]

[1]Helmholtz Institute Ulm (HIU), Ulm, Germany

[2]Karlsruhe Institute of Technology (KIT), Karlsruhe, Germany

[3]Department of Chemistry, KU Leuven, Leuven, Belgium

[4]Department of Energy Convergence Engineering, Cheongju University, Cheongju, Republic of Korea

[5]Chemistry Department, Sapienza University of Rome, Rome, Italy

Correspondence
Guk-Tae Kim and Stefano Passerini, Helmholtz Institute Ulm (HIU), Helmholtzstrasse 11, Ulm 89081, Germany.
Email: guk-tae.kim@kit.edu and stefano.passerini@kit.edu

Funding information
China Scholarship Council; European Commission, Grant/Award Number: 875557; Helmholtz-Gemeinschaft; National Research Foundation of Korea, Grant/Award Numbers: NRF-2021R1A4A200168711, NRF-2020R1A2C2009057, 2021R1A4A2001687, P0011933

Abstract

High-voltage nickel-rich layered cathodes possess the requisite, such as excellent discharge capacity and high energy density, to realize lithium batteries with higher energy density. However, such materials suffer from structural and interfacial instability at high voltages (>4.3 V). To reinforce the stability of these cathode materials at elevated voltages, lithium borate salts are investigated as electrolyte additives to generate a superior cathode-electrolyte interphase. Specifically, the use of lithium bis(oxalato)borate (LiBOB) leads to an enhanced cycling stability with a capacity retention of 81.7%. Importantly, almost no voltage hysteresis is detected after 200 cycles at 1C. This outstanding electrochemical performance is attributed to an enhanced structural and interfacial stability, which is attained by suppressing the generation of micro-cracks and the superficial structural degradation upon cycling. The improved stability stems from the formation of a fortified borate-containing interphase which protects the highly reactive cathode from parasitic reactions with the electrolyte. Finally, the decomposition process of LiBOB and the possible adsorption routes to the cathode surface are deduced and elucidated.

KEYWORDS

cathode electrolyte interphase, electrolyte additive, high voltage cathodes, LiBOB, nickel-rich cathodes

1 | INTRODUCTION

Pursuing higher energy density is one of the main driving forces for current lithium-ion and lithium-metal batteries.[1] The energy density is mainly dependent on the cell voltage and discharge capacity.[2] Generally, for transition metal layered oxides ($LiNi_{1-x-y}Co_xMn_yO_2$, abbreviated as NCM), research efforts have targeted cell capacity improvements by increasing the nickel content.[3,4] Recently, another approach has emerged for targeting

This is an open access article under the terms of the Creative Commons Attribution License, which permits use, distribution and reproduction in any medium, provided the original work is properly cited.
© 2023 The Authors. *InfoMat* published by UESTC and John Wiley & Sons Australia, Ltd.

higher energy density by extending high charge voltages beyond 4.3 V, especially for the conventional $LiCoO_2$ cathode.[5,6] However, the elevated cut-off voltage induces performance degradation because of extensive cation mixing owing to the similar ionic radius of Li^+ and Ni^{2+} (e.g., irreversible capacity loss and voltage decay), which is even more severe for nickel-rich cathodes, and the generation of microcracks.[7–9] The latter is likely ascribed to the high surface reactivity of the deeply delithiated cathode at high voltages, as the initially formed cathode–electrolyte interphase (CEI) passivation layer is not sufficiently robust to hinder the continuous side reactions with conventional carbonate electrolytes.[10,11] For this reason, coating the cathode surface with a protective layer[12–14] or exploiting a high voltage electrolyte system[15–18] are two possible approaches to improve the performance of such cathodes at elevated potentials.

In recent years, the in situ formation of a stable CEI has been considered as a promising strategy to enhance the interfacial stability because it is an effective and low-cost route to improve the electrochemical performance without requiring substantial changes of the battery production chain.[19,20] Thus far, most research activities focused on fluorine-containing species such as fluoroethylene carbonate (FEC)[21,22] and (methyl(2,2,2-trifluoroethyl) carbonate) (FEMC)[23] or phosphorus-based additives such as tripropargyl phosphate (TPP)[24,25] and tris(trimethylsilyl) phosphite (TMSP).[26,27] Besides, boron-containing molecules have also been studied as electrolyte additives for LIBs. For instance, Wang et al.[20] designed a F-rich and B-rich CEI layer on $LiNiO_2$, achieving a high capacity retention of >80% after 400 cycles with a cut-off voltage of 4.4 V. They reported that the F-rich and B-rich CEI layer prevented continuous side reactions at the CEI, hindering the structural transition to an inactive rock-salt (NiO) phase. Kang et al.[28] constructed a hierarchical CEI layer using lithium difluoro (oxalato)borate (LiDFOB) as electrolyte additive, realizing a LiF-rich inner layer and an organic outer layer, thus, obtaining a capacity retention of 69.8% after 400 cycles with a cut-off voltage of 4.3 V. Despite these promising results, current research activities on boron-containing additives for Ni-rich cathodes have centered on conventional cut-off voltages rather than elevated cut-off voltages. Boron-containing additives are widely used in combination with high-voltage cathodes such as $LiNi_{0.5}Mn_{1.5}O_4$[29,30] and Li-rich cathodes,[31–33] but not with Ni-rich NCM cathodes with elevated cut-off voltages. Nonetheless, these findings suggest that boron-based additives could also be beneficial for high-voltage NCM. Herein, lithium borate additives are investigated in combination with high cut-off voltages (≥4.6 V) and Ni-rich NCM cathodes in lithium-metal batteries.

2 | RESULTS AND DISCUSSION

In this work, the Ni-rich cathode material $LiNi_{0.83}Co_{0.1}Mn_{0.05}B_{0.01}O_2$ (NCM83) was used. The characterization by x-ray diffraction (XRD) pattern is presented in Figure S1, revealing the expected layered structure. First, the effect of extending the upper cut-off voltage for the Ni-rich cathode was evaluated. For this purpose, the cells were cycled at two different voltages of 4.3 and 4.6 V. The first charge/discharge profile is presented in Figure 1A. The two curves are practically overlapping until 4.3 V. For the electrode tested up to 4.6 V, a relatively steep increase in potential is observed, which releases an additional capacity of about 20 mAh g^{-1}. This additional specific capacity is also obtained during the subsequent discharge process, resulting in the initial Coulombic efficiency (CE) of ~92.0%, that is, equal to that of the cell charged to 4.3 V. The plot of the differential capacity provides more information about the effect of a higher cut-off voltage upon charge (Figure 1B). The exceeding part (evidenced by the green circle) is associated to the phase transition from the H3 phase (O3 layer stacking) to the H4 hexagonal phase (O1 stacking).[34] Figure 1C shows a comparison of the differences in specific capacity and specific energy achieved by the cells cycled up to 4.3 and 4.6 V. At charge rates of 0.1C and 1C (1C = 200 mA g^{-1}), the discharge capacity increases by 8.7% (0.1C) and 8.0% (1C), elevating the cut-off voltage from 4.3 to 4.6 V. The specific energy rises by 9.6% at 0.1C and reaches a maximum specific energy of more than 900 Wh kg^{-1}. However, this initial gain in specific capacity and energy comes at the expense of cycling stability (Figure 1D), with the capacity retention decreasing from 86.1% (4.3 V) to 73.1% (4.6 V) after 200 cycles. Additionally, a rapid decay of the average discharge voltage was observed (Figure 1E), which has been ascribed to the structural transformation from the layered phase to the rock-salt phase.[35] This process is schematically depicted in Figure 1F. The extended delithiation at elevated potentials results in the formation of a greater proportion of lithium vacancies in the cathode structure. As a result, aggravating the migration of Ni^{2+} ions from the transition metal layer into these lithium vacancies in the deeply delithiated state owing to the similar ionic radius of Ni^{2+} and Li^+. This results in an inactive rock-salt structure and structural distortion on the surface and this phase transition can spread from the external surface to the interior surface along the microcracks irritated by the highly anisotropic strain,[36] which hinders the intercalation of lithium ions.[37,38] Besides, the elevated cut-off voltage increases the formation of highly reactive Ni^{4+}, which accelerates the electrolyte decomposition and the formation of a thicker CEI layer. This leads to a great increase in resistance for lithium transport.[15,39]

25673165, 0, Downloaded from https://onlinelibrary.wiley.com/doi/10.1002/inf2.12462 by Karlsruher Inst F. Technologie, Wiley Online Library on [03/07/2023]. See the Terms and Conditions (https://onlinelibrary.wiley.com/terms-and-conditions) on Wiley Online Library for rules of use; OA articles are governed by the applicable Creative Commons License

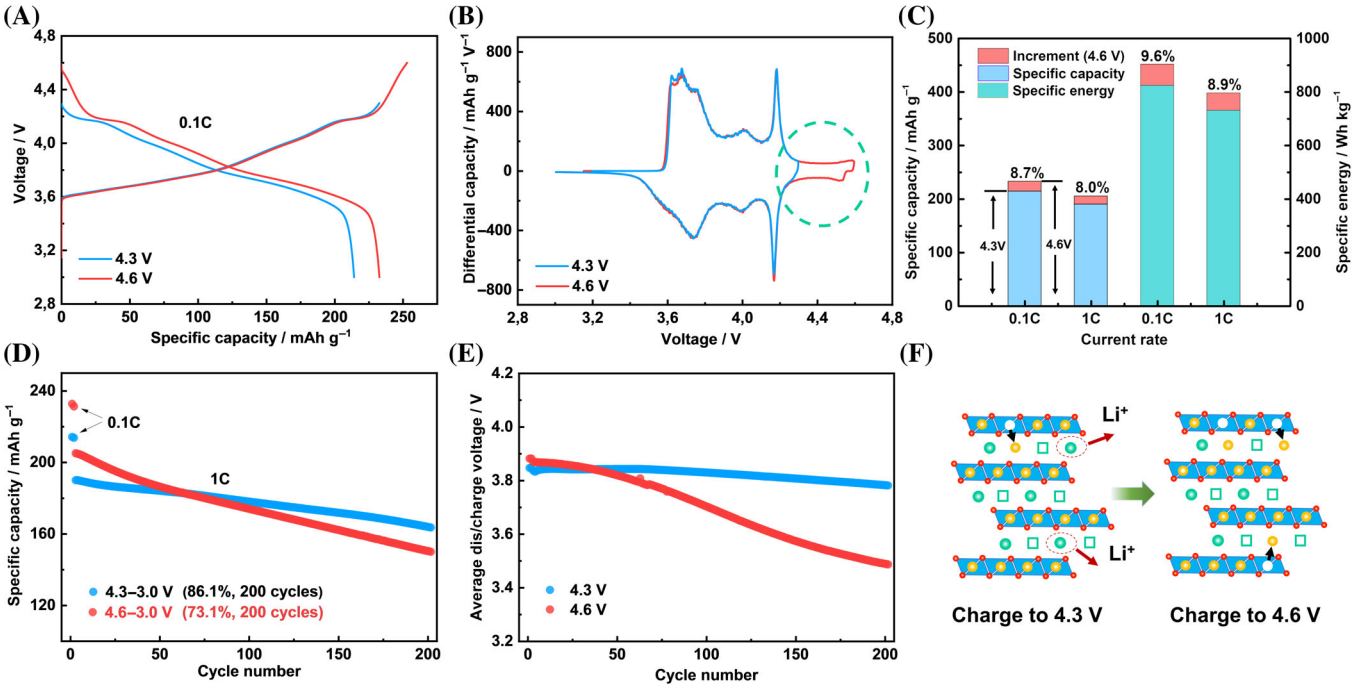

FIGURE 1 Electrochemical behavior of NCM83 cathodes upon cycling to different upper cut-off voltages (4.3 or 4.6 V). (A) Charge/discharge voltage profile and (B) differential capacity plot for the first cycle at 0.1C; (C) comparison of the specific capacity and energy for the two upper cut-off voltages; (D) cycling behavior and (E) average discharge voltage for the two different upper cut-off voltages; (F) schematic illustration of the structural transition at elevated potentials.

To further examine the impact of the increased cut-off voltage, the NCM83 electrodes were investigated after 200 cycles by ex situ scanning electron microscopy (SEM) and ex situ x-ray photoelectron spectroscopy (XPS). The morphology of the NCM83 particles on the electrodes surface reveals some differences. A large fraction of the secondary spherical particles have undergone severe pulverization after the long-term charge/discharge process up to 4.6 V (Figure S2), while no changes were detected in the electrode tested up to 4.3 V apart from a few micro-cracks. These changes are even more apparent when comparing images with higher magnification as shown in Figure 2A,E,I. The complete pulverization of the particles originates from the strong strain at such high potentials,[40,41] eventually causing severe capacity fading. This structural instability is generally ascribed to a brittle electrode/electrolyte interphase.[15,40] Therefore, the surfaces of the electrodes were also characterized by ex situ XPS after 200 cycles, as shown in Figure 2. By comparing the spectra of the pristine and cycled electrodes, the most evident difference is a very strong peak at around 685.0 eV in the F1s detail spectrum of the electrode cycled up to 4.3 V, which is associated to LiF. In principle, this is a beneficial component to the CEI layer.[42] However, the high intensity of the LiF peak also indicates an extensive thickness of the CEI layer on the cathode surface, originating from an extensive (possibly continuous) electrolyte decomposition,[43] which is still detected even after removing ~3 nm of the topmost layer by Ar^+ ion sputtering (Figure S3). The larger thickness of the CEI layer is also indicated by the disappearance of the C–F peak at 291.0 eV in the C1s region and at 688.1 eV in the F1s region, which are characteristic for the CF_2 groups of the PVdF binder, and the weakening of the M–O (M: Ni, Co, Mn) peak in the O1s region related to transition metal oxides. In contrast, the electrode subjected to a higher cut-off voltage (4.6 V) displays a lower intensity of the Li–F peak, while those peaks related with the PVdF binder and the M–O bond are still visible. This unexpected result may be explained by a more pronounced deposition of organic species (e.g., lithium alkyl carbonates [$ROCO_2Li$]) besides the inorganic species (LiF), which is indicated by the higher intensity of the corresponding peaks at ~289.0 eV (C1s region) and ~531.9 eV (O1s region). This result suggests that the organic solvents are decomposed to a greater extent at higher cut-off voltages, resulting in a more organic (and likely less dense) CEI layer, which increases the charge transfer resistance and, thus, the cell polarization. Additionally, it might be that part of the CEI is oxidized at such high potentials.[44] As a consequence, the formed CEI layer on the cathode surface has a pronounced impact on the cathode structure and electrochemical performance.

25673165, 0, Downloaded from https://onlinelibrary.wiley.com/doi/10.1002/inf2.12462 by Karlsruher Inst F. Technologie, Wiley Online Library on [03/07/2023]. See the Terms and Conditions (https://onlinelibrary.wiley.com/terms-and-conditions) on Wiley Online Library for rules of use; OA articles are governed by the applicable Creative Commons License

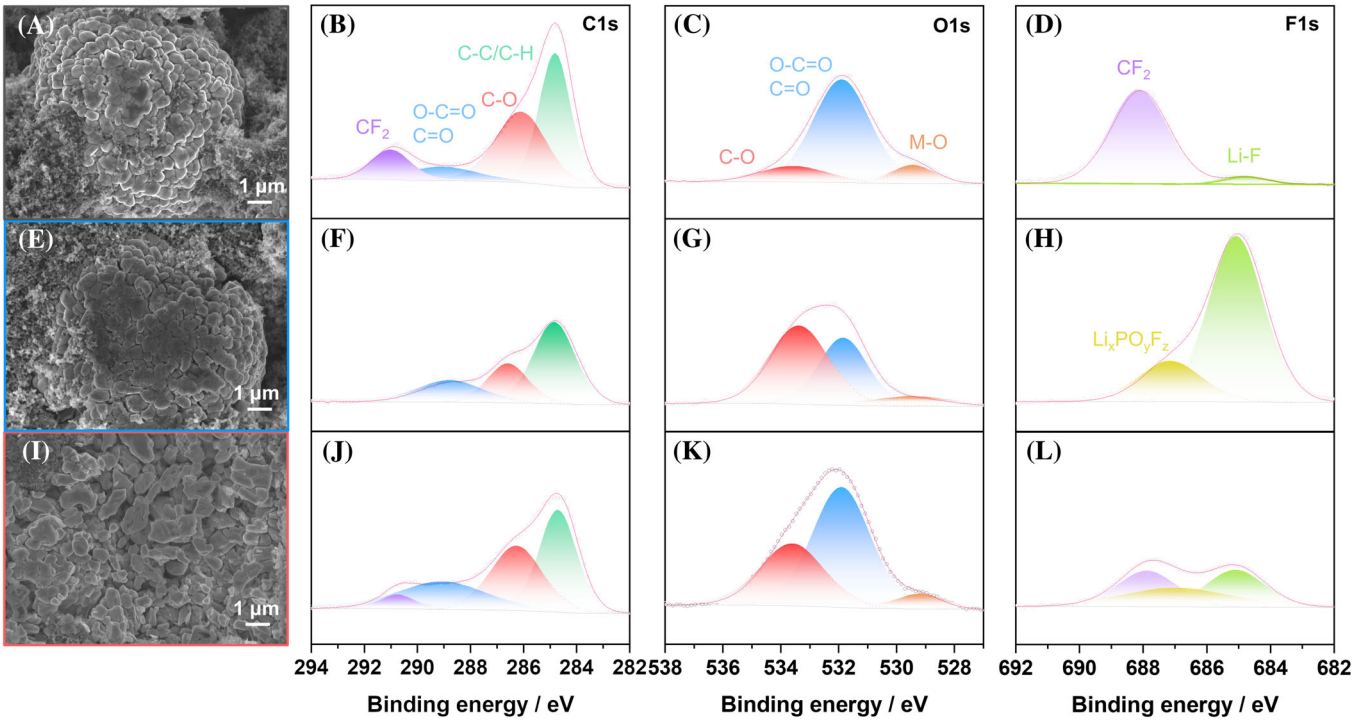

FIGURE 2 SEM micrographs and XPS detail spectra in the C1s, O1s, and F1s region of the pristine electrode (A–D) and electrodes cycled with a cut-off voltage of 4.3 V (E–H) and 4.6 V (I–L).

To reinforce the CEI layer, lithium bis(oxalato)borate (LiBOB) was selected as the electrolyte additive since it is known to anodically decompose prior to the organic solvent, forming an interlayer containing B-O.[1] To verify this, the electrochemical stability of the commercial organic electrolyte (LP30, 1 M $LiPF_6$ in EC/DMC) with/without LiBOB as additive was investigated by linear sweep voltammetry (LSV), as shown in Figure 3A. The profiles demonstrate that the oxidation peak occurs slightly earlier for the electrolyte with LiBOB than the neat LP30, in agreement with the highest occupied molecular orbital (HOMO) energy level of LiBOB with respect to the other electrolyte components.[45] The decomposition of LiBOB generates a borate-containing layer on the surface of the cathode particles, which helps to suppress side reactions between the electrolyte and the cathode.[1,32] Two-electrode Li/NCM83 cells were assembled to evaluate the electrochemical performance of the positive electrode without and with LiBOB as additive. First, to optimize its content, a series of electrolytes containing 0.5, 1.0, and 1.5 wt% LiBOB in LP30 were prepared. These electrolytes were employed in Li/NCM83 cells; electrochemical performance are compared in Figure S4. The cells with 0.5 and 1.0 wt% LiBOB showed similar cycling stability initially, while the latter displays superior performance across the whole 200 cycle test. Presumably, the CEI formed in the presence of 1.0 wt% LiBOB is more robust ensuring improved long-term cycling performance when elevating the upper cut-off to 4.6 V. When increasing the amount of LiBOB to 1.5 wt%, the cell showed a lower capacity and inferior cycling stability since the beginning of the test, which is probably due to the excess of highly resistant borate-containing components forming in the CEI or SEI layer, resulting in higher interfacial resistance that hinders lithium diffusion across the interface.[10,46] Taken together, 1.0 wt% LiBOB was optimal for an upper cut-off voltage of 4.6 V. The first charge/discharge profiles (with an upper cut-off voltage of 4.6 V) are compared in Figure 3B. The sharp increase of the voltage in the initial stage is ascribed to the spontaneous reduction of BOB^- in contact with the lithium metal anode, which occurs prior to the beginning of the test and generates a more resistive solid electrolyte interphase (SEI) on the negative electrode.[47] After the steep initial increase, the charge profile converges with the profile of the cell comprising the electrolyte without the additive. The overlapping charge profiles at elevated voltages, also indicates that the BOB^- oxidation takes place at the beginning of the charge process, that is, before the overlap of the two voltage profiles. The BOB^- oxidation is also evident from the lower initial CE of the cell compared with that with the additive-free electrolyte (90.1% vs. 92.0%). However, when comparing the subsequent cycles (Figure 3C), it is apparent that the cycling stability is significantly increased by adding LiBOB in the electrolyte, resulting in a superior capacity retention of

25673165, 0, Downloaded from https://onlinelibrary.wiley.com/doi/10.1002/inf2.12462 by Karlsruher Inst F. Technologie, Wiley Online Library on [03/07/2023]. See the Terms and Conditions (https://onlinelibrary.wiley.com/terms-and-conditions) on Wiley Online Library for rules of use; OA articles are governed by the applicable Creative Commons License

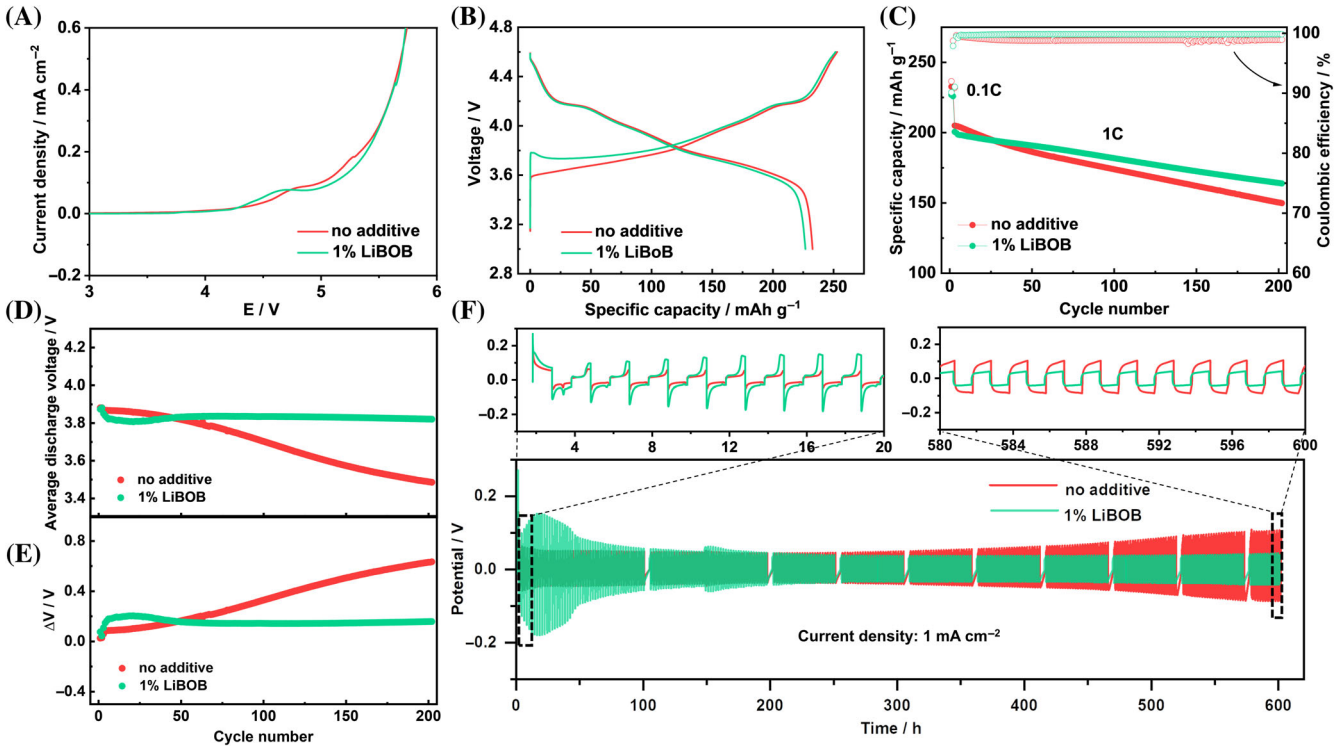

FIGURE 3 (A) Linear sweep voltammetry experiments conducted in Li//Pt cells comprising the base LP30 electrolyte with and without 1 wt% LiBOB (sweep rate: 0.1 mV s^{-1}). (B) 1st cycle dis-/charge profiles of Li//NCM83 cells with and without the additive. (C) Plot of the specific capacity vs. the cycle number for these cells. (D) Plot of the average discharge voltage. (E) Plot of the voltage hysteresis between the average charge and discharge. (F) Stripping/plating tests conducted in symmetric Li/Li cells comprising the LP30 electrolyte with and without 1 wt% LiBOB (current density: 1 mA cm^{-2} for 1 h per stripping/plating step); magnifications of the framed regions are provided on top.

81.7% compared with 73.9%. Notably, the addition of LiBOB also has a positive effect for the lower cut-off voltage of 4.3 V, improving from 86.1% to 91.3% (Figure S5). To evaluate whether this beneficial effect is generally observed for boron-containing lithium salts, LiDFOB was also tested as electrolyte additive (Figure S6). However, unlike LiBOB, adding LiDFOB to the electrolyte resulted in inferior cycling stability with only 57.7% capacity retention after 200 cycles. Hence, this positive effect is distinct to LiBOB.

Subsequently, the average discharge voltage was calculated to evaluate the structural degradation of the cathode and the cell polarization (Figure 3D). Interestingly, the average discharge voltage of the cells employing the electrolyte with/without LiBOB additive exhibits differing trends. For the former cells, the average discharge voltage is more stable during the initial cycles, followed by a dramatic decrease, suggesting a significant structural transformation in the nickel-rich cathodes, due to the ongoing Li^{+}/Ni^{2+} mixing during the high-voltage charge/discharge process. In contrast, the average discharge of the cell with the LiBOB additive shows a relatively steep drop initially, followed by a very stable average discharge voltage for the remaining cycles, demonstrating that the reinforced CEI layer effectively protects the cathode particles from such detrimental structural changes. Further, the voltage hysteresis ΔV, that is, the difference between the average charge and discharge voltage, was compared (Figure 3E). In agreement with the behavior of the average discharge voltage, ΔV is continuously increasing in the cells without the additive, while it remains very stable (after an initial slight increase and then relaxation) in the presence of LiBOB. To investigate the impact of the lithium-metal counter electrode and its interface with the electrolyte—that is, the SEI formed at the interface with the lithium-metal electrode—symmetric Li||Li cells were assembled and subjected to lithium stripping/plating tests (Figure 3F). The cells show a similar behavior, with the overpotential initially increasing, before decreasing again and then stabilizing for the cell comprising LiBOB additive, while it is initially stable, but continuously increases after few cycles in the absence of LiBOB. This suggests that the SEI formed in the presence of LiBOB is more stable upon stripping and plating than that formed without LiBOB, which appears to continuously grow. To further evaluate the evolution of the SEI, electrochemical

25673165, 0, Downloaded from https://onlinelibrary.wiley.com/doi/10.1002/inf2.12462 by Karlsruher Inst F. Technologie, Wiley Online Library on [03/07/2023]. See the Terms and Conditions (https://onlinelibrary.wiley.com/terms-and-conditions) on Wiley Online Library for rules of use; OA articles are governed by the applicable Creative Commons License

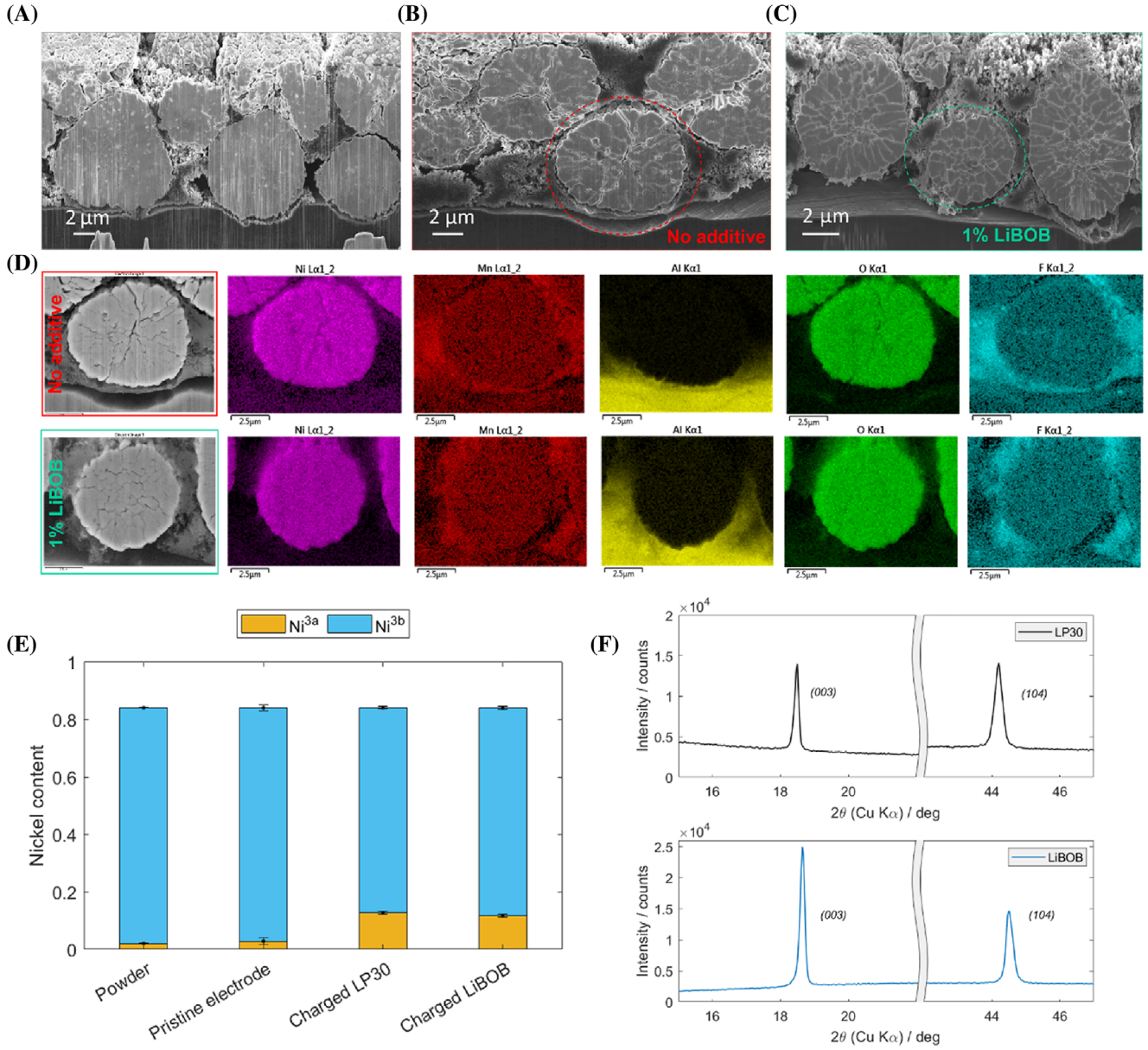

FIGURE 4 Cross-sectional SEM micrographs of (A) a pristine NCM83 electrode, (B) a cycled NCM83 electrode using neat LP30, and (C) LP30 with 1 wt% LiBOB. (D) EDX mapping of the cross section of the cycled NCM83 particles using neat LP30 (top) and the LiBOB-containing electrolyte (bottom). (E) Nickel content for the pristine powder and electrode as well as the cycled electrodes with and without the additive, divided into Ni^{3a} (Li-interslab layer) and Ni^{3b} (NCM83-intraplanar layer) based on the results of Rietveld refinement. (F) Magnifications of the (003) and (104) reflections recorded for the cycled electrodes without (top) and with (bottom) 1 wt% LiBOB.

impedance spectroscopy (EIS) was performed (Figure S7). The resulting spectra corroborates this trend, revealing a continuous increase in impedance for the neat electrolyte, while it is decreasing and stabilizing for the cell comprising the LiBOB electrolyte additive. Hence, it is concluded that adding LiBOB to the electrolyte also has a beneficial effect on the SEI at the lithium-metal negative electrode, which contributes to the superior cycling stability of the Li||NCM83 cells. This result can be confirmed by the SEM micrographs of cycled lithium metal anodes in Figure S8; some cracks and lithium dendrites are evident on the lithium metal surface without LiBOB, resulting in an unstable lithium/electrolyte interface. In contrast, the lithium metal surface with LiBOB additive appears more rigid and smoother.

To determine the effect of LiBOB on the cathode side, the cycled electrodes were characterized by cross-sectional scanning electron microscopy (SEM) and energy-dispersive x-ray (EDX) spectroscopy. Figure 4A–C shows the comparison of the cross-section of pristine and cycled electrodes employing the LP30 electrolyte as such and with 1.0 wt% LiBOB as additive. The SEM micrographs obtained for the

25673165, 0, Downloaded from https://onlinelibrary.wiley.com/doi/10.1002/inf2.12462 by Karlsruher Inst F. Technologie, Wiley Online Library on [03/07/2023]. See the Terms and Conditions (https://onlinelibrary.wiley.com/terms-and-conditions) on Wiley Online Library for rules of use; OA articles are governed by the applicable Creative Commons License

pristine electrode (Figure 4A) show the shape of intact NCM83 particles. Differently, the NCM83 particles cycled with the baseline LP30 electrolyte (Figure 4B) show several large microcracks inside the particles. These are substantially reduced in the case of the NCM83 particles cycled with LiBOB (Figure 4C), confirming that the additive suppresses the structural degradation at elevated cut-off voltages. The SEM micrographs of the cathode electrode surface also demonstrate a more severe pulverization of the NCM83 particles in LP30 electrolyte than with LiBOB (Figure S9), which results from the accumulation of microcracks during the continuous charge/discharge process. Such microcracks when protruding to the outer surface of the secondary particle favor additional side reactions with the electrolyte leading to higher irreversible capacity and pronounced structural degradation.[36,48] The EDX mapping results (Figure 4D) further support these findings: in the case of the baseline LP30 electrolyte, a relatively inhomogeneous Ni distribution was observed along the microcracks and at the surface, as well as a high fluorine concentration along the microcracks resulting from the pronounced electrolyte decomposition. The structural degradation and cation mixing were further studied by ex situ XRD and Rietveld refinement (Figures 4E and S10, and Tables S1–S3). In the latter, Ni was allowed to occupy the Li-interslab layer (Ni^{3a}) and the NCM83 intraplanar layer (Ni^{3b}), fixing its total content to 0.83 as determined by ICP-OES. While the cation mixing is negligible for the NCM83 powder and the pristine electrode, as displayed in Figure 4E, the degree of cation mixing increased significantly in the cycled electrodes. However, the electrode in contact with neat LP30 showed a much higher cation mixing than the one cycled in the presence of LiBOB (0.16 Ni^{3a} for LP30 vs. 0.11 Ni^{3a} for LiBOB; see also Table S1–S3). The degree of cation mixing can also be qualitatively determined by observing the ratio of the (*003*) and (*104*) reflections.[49,50] The difference of the peak ratio determined for the charged samples is presented in Figure 4F, supporting a higher cation mixing in the LP30 sample, which eventually causes the structural degradation of the NCM83 cathode.[51] Further results of the Rietveld refinement, including the refined lattice and atomic parameters, can be found in Tables S1–S3.

To further study and compare the phase transitions during the first cycle, operando XRD measurements were conducted (Figure S11). For both electrolyte formulations (with and without LiBOB), a pronounced shift of the (003), (006), (104), and (108) reflections is noted in the highly delithiated state, indicating a high strain occurring in the NCM83 particles. However, there are no significant differences for the two cells, indicating that the structural evolution of the NCM83 particles is occurring continuously upon cycling (as also suggested by the fading behavior of the cells) rather than prominently in the first cycle.

Therefore, we investigated the plots of the differential capacity (dQ/dV) and their evolution upon cycling in more detail (Figure 5A,B). The plots of the cell comprising the baseline LP30 electrolyte (Figure 5A) show a large peak shift of the redox feature associated with the H1 ⇆ M phase transition toward higher potentials, indicating a high degree of cation mixing.[52] Simultaneously, the disappearance of the H2 + H3 phase upon cycling suggests a decreasing reversibility of the H2 ⇆ H3 phase transition. These findings are commonly associated to the formation of an inactive rock-salt NiO layer on the particle surface, which is hindering lithium ion de-/insertion.[48] In contrast, no substantial peak shift or disappearance of redox peaks was observed when LiBOB was added to the electrolyte (Figure 5B), but only a small decline in the H2 + H3 region. The accompanying EIS analysis (Figure 5C,D) supports these findings. The additive-free cell showed a continuous growth of the impedance with cycling (Figure 5C), which did not occur when LiBOB was added (Figure 5D) suggesting that the irreversible phase transition to NiO is greatly suppressed in this case.

Finally, the impact of LiBOB on the CEI composition was investigated by ex situ XPS measurements of a cycled electrode on the surface and after removing ~3 nm of the topmost layer by Ar^+ ion sputtering (Figure 6). Different from the spectra of the electrodes cycled in the baseline LP30 electrolyte (Figure 2K), a strong peak at 533.3 eV was detected in the O1s region (Figure 6A), which can mainly be associated to LiBOB, demonstrating the involvement of BOB^- into the CEI layer. In the B1s region (Figure 6B), two B contributions could be discerned, but also the P2s peak of phosphates formed by decomposition of PF_6^- (full details are presented in Section 4). The peak at higher binding energy (193.2 eV) is assigned to LiBOB,[20] the one at lower binding energy (192.2 eV) is at least in part due to the BO_3^{3-} dopant in the electrode material (cf. B1s detail spectrum of the pristine electrode, Figure S12). In addition, LiBOB decomposition products (Li_xBO_y) may contribute to this peak. After sputtering, the intensity of the LiBOB features decreased in both the O1s and B1s region, and the oxalate peak (290.0 eV) was also strongly reduced in the C1s detail spectrum (Figure S13). Interestingly, the B1s peak due to LiBOB decomposition products (Li_xBO_y) (and of BO_3^{3-} from the electrode active material) increased in intensity after sputtering. The growth of this B1s peak is more pronounced than that of other features related to the electrode material (e.g., Ni2p), besides, there is a larger atomic ratio increase of boron element before and after sputtering with LiBOB additive than without LiBOB additive (Table S4), hence a growing

25673165, 0, Downloaded from https://onlinelibrary.wiley.com/doi/10.1002/inf2.12462 by Karlsruher Inst F. Technologie, Wiley Online Library on [03/07/2023]. See the Terms and Conditions (https://onlinelibrary.wiley.com/terms-and-conditions) on Wiley Online Library for rules of use; OA articles are governed by the applicable Creative Commons License

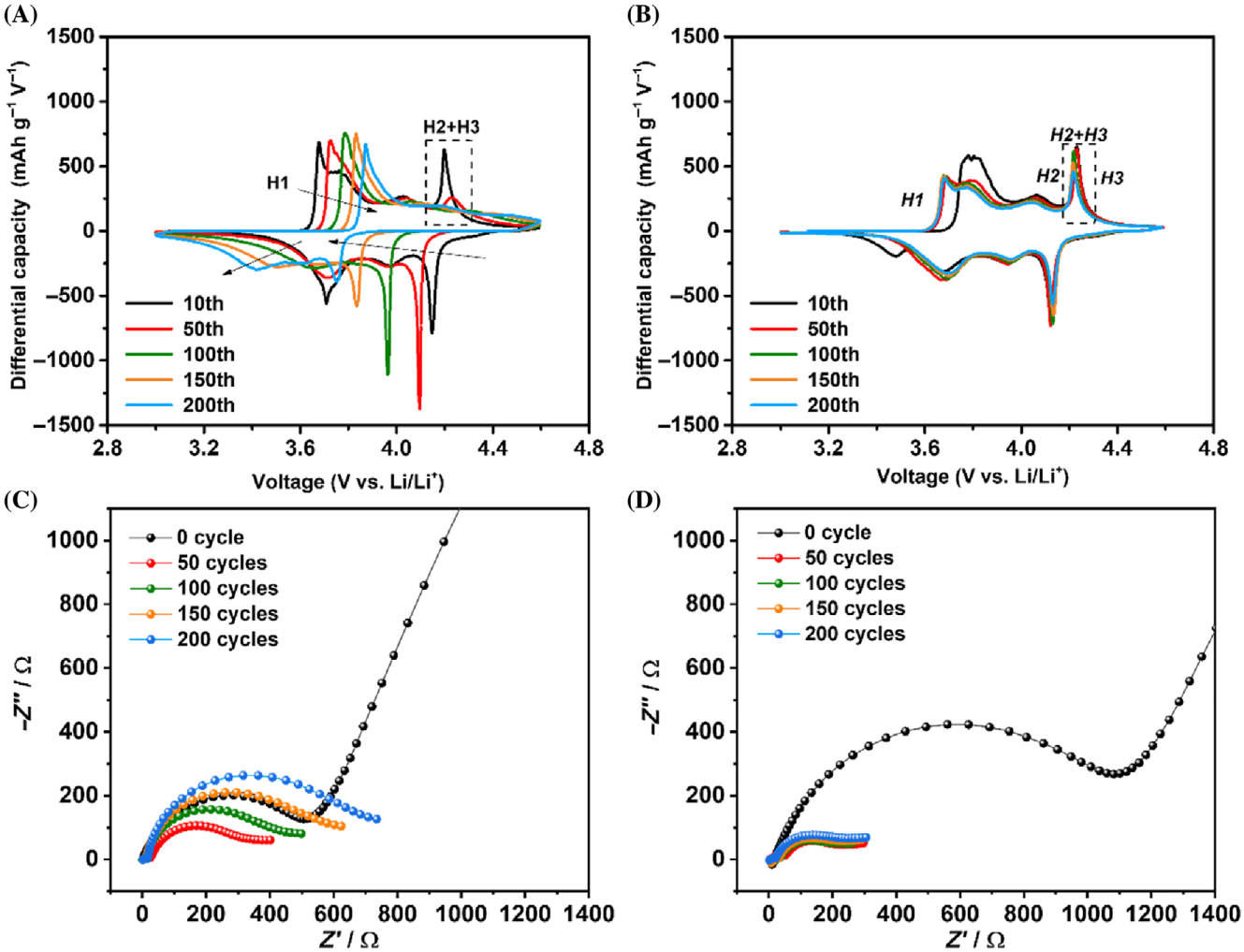

FIGURE 5 Evolution of the differential capacity plot upon cycling of Li/NCM83 cells comprising (A) the baseline LP30 and (B) additionally LiBOB. Evolution of the impedance upon cycling for (C) the neat electrolyte and (D) the LiBOB-containing electrolyte.

contribution of Li_xBO_y species after sputtering seems plausible. The counteracting development of the intensities points to a change of the predominant B species in the CEI from LiBOB in the outer layer to its decomposition products (Li_xBO_y) in the inner layer. This result indicates that LiBOB was decomposed during the initial cycling, and it is also the reason why the cycling behavior becomes gradually steady after a few cycles. Finally, the F1s region shows a significant increase of the LiF peak intensity after sputtering indicating that the $LiPF_6$ salt decomposed initially. With the growing CEI layer thickness upon further cycling, this side reaction was suppressed, and consequently the content of LiF in the CEI layer decreases.

The XPS results have proven the presence of borate containing species in the CEI layer, nevertheless, the role of the LiBOB additive and its contribution to CEI layer and its absorption onto the cathode surface are unclear. Hence, based on previous studies,[31,32,53] the possible decomposition route of LiBOB was deduced as shown in Figure 7A. The adsorption energy of decomposition product on different sites of cathode was calculated using density functional theory (DFT, see details in Section 4) calculations (Figure 7B). First, a BOB^- anion near the NCM83 cathode surface loses an electron at high voltage,[31] causing the B–O bond to break, that is, resulting in the ring opening. The unstable C_2O_4 group further decomposes resulting in the generation of CO_2 gas. The boron atom remains in the oxalatoborate radical (1OB) which is highly reactive and attacks ethylene carbonate (EC) to form 1OB-EC structure,[31,32] yielding a final boron-containing polymer on the electrode surface. Regarding the inclusion of the boron-containing decomposition products in the CEI, the DFT calculations were utilized to evaluate the adsorption energy between the decomposition products and the cathode surface. Accounting for the potentially different boron-containing products, the most representative product, 1OB-EC, was chosen. The calculated 1OB-EC adsorption energies on

25673165, 0, Downloaded from https://onlinelibrary.wiley.com/doi/10.1002/inf2.12462 by Karlsruher Inst F. Technologie, Wiley Online Library on [03/07/2023]. See the Terms and Conditions (https://onlinelibrary.wiley.com/terms-and-conditions) on Wiley Online Library for rules of use; OA articles are governed by the applicable Creative Commons License

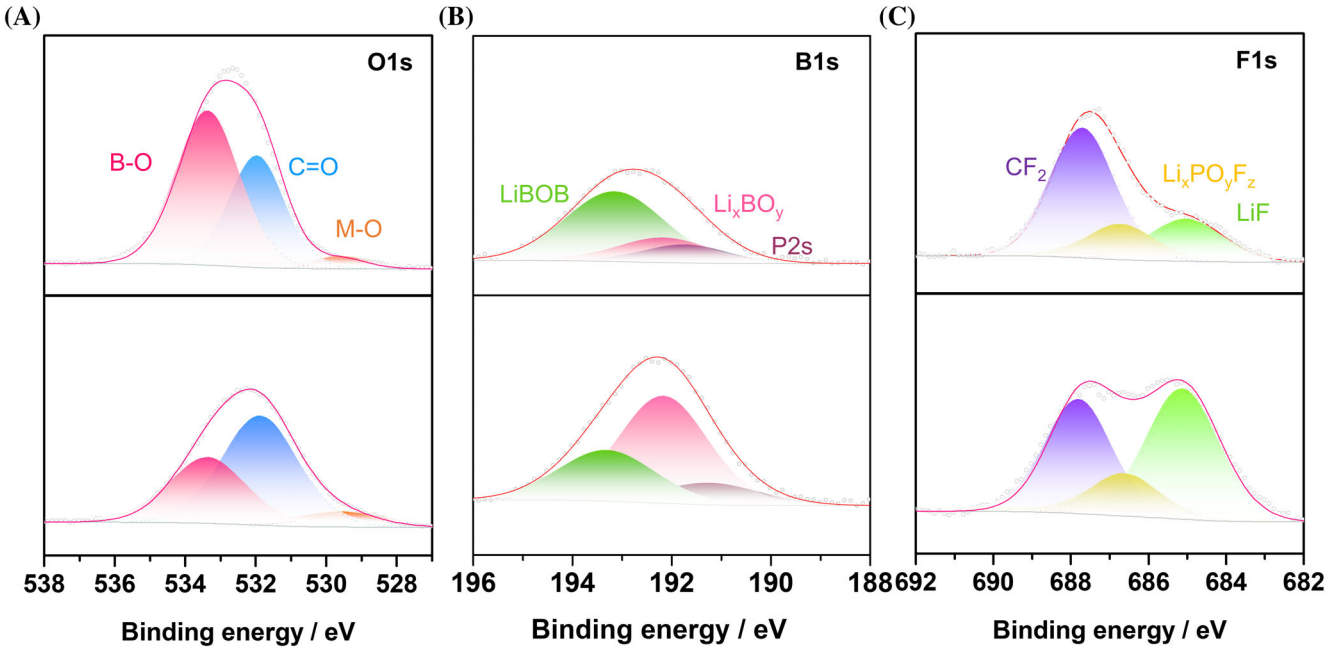

FIGURE 6 XPS analysis of NCM83 electrode in the O1s (A), B1s (B), and F1s region (C) after cycling up to 4.6 V in LP30 electrolyte with 1 wt% LiBOB additive (top: before sputtering, bottom: after sputtering).

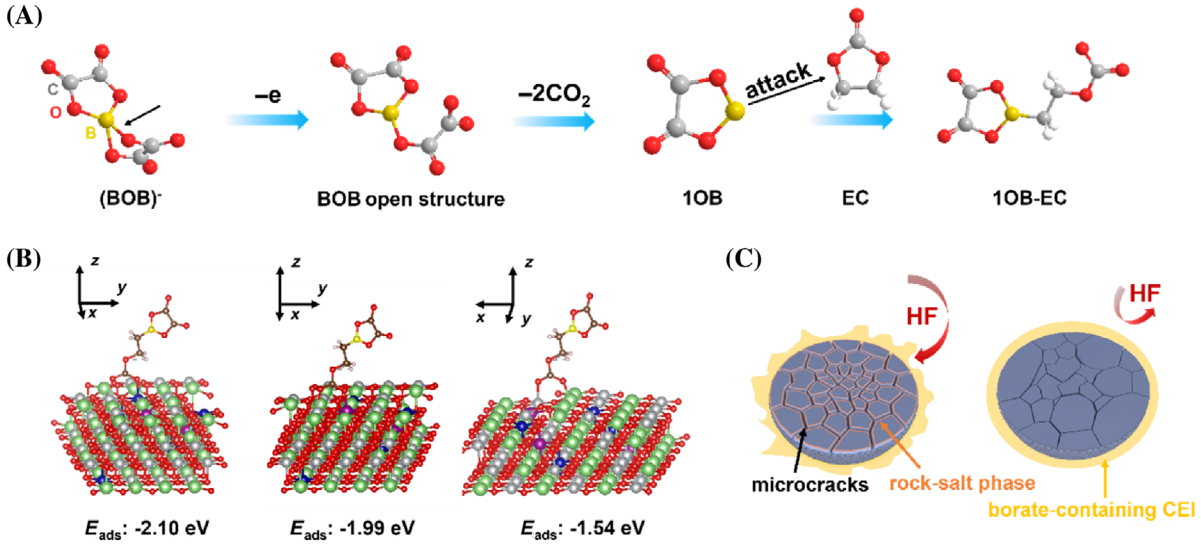

FIGURE 7 (A) Proposed decomposition route of BOB^- during cycling at high voltage (4.6 V). (B) Possible adsorption sites and energy between LiBOB and NCM83 cathode (nickel: gray balls, cobalt: blue balls, manganese: purple balls, lithium: green balls, boron: yellow balls), (C) Schematic illustration of the electrode morphology and CEI of NCM83 particles upon cycling in LP30 (left) and LP30 + 1.0 wt% LiBOB (right).

the NCM83 surface (Figure 7B) are negative for three sites, that is, bidentate coordination with Ni–Co, Ni–Mn, and Ni–Li, indicating that the 1OB-EC group may absorb on the NCM83 surface rather than dissolving into the electrolyte. The lower (i.e., more negative) values of the Ni–Co and Ni–Mn absorption sites suggest that they are the most favorable. For comparison, the adsorption energy of EC molecule was also calculated and produces a less negative value (Figure S14), demonstrating the adsorption of NCM83 cathode to 1OB-EC is much stronger than EC molecule. The further decomposition reaction involving additional EC molecules (i.e., 1OB-2EC, 1OB-3EC, ...) has a limited effect on the adsorption energies. Therefore, it can be predicted that the longer-chain decomposition products will also absorb on the electrode, resulting in the generation of a robust and uniform CEI

25673165, 0, Downloaded from https://onlinelibrary.wiley.com/doi/10.1002/inf2.12462 by Karlsruher Inst F. Technologie, Wiley Online Library on [03/07/2023]. See the Terms and Conditions (https://onlinelibrary.wiley.com/terms-and-conditions) on Wiley Online Library for rules of use; OA articles are governed by the applicable Creative Commons License

layer. This suppresses the HF attack to the NCM83 particles' surface reducing the microcracks generation and the rock-salt layer formation, originating from the cation mixing spreading along the microcracks (Figure 7C), and contributing to the superior cycling stability of the Li||NCM83 cells, which is comparable to the state-of-art performances of other high voltage nickel-rich cathodes which have been recently reported (Table S5).

3 | CONCLUSION

In this work, the use of LiBOB as electrolyte additive in cells consisting of the high-voltage nickel-rich (NCM83) positive electrode and lithium metal, has been thoroughly investigated. First, the benefits and drawbacks resulting from extending the high cut-off voltage of the nickel rich cathode were evaluated. Subsequently, it was demonstrated that the use of LiBOB additive in the conventional LP30 electrolyte enables improved cycling stability (up to 81.7% vs. 73.9% for neat LP30) upon 200 cycles at 1C. Importantly, the LiBOB additive displayed an unexpected high stability of the cell voltage originating from the formation of a peculiar CEI. This interphase was investigated using various characterization methods, revealing the reduced formation of microcracks resulting from the generation of the borate containing CEI causing fewer irreversible phase transformations in the bulk of NCM83. This work highlights the possibility to break through the capacity bottleneck of nickel-rich cathodes and achieve high-energy-density lithium-metal battery.

4 | EXPERIMENTAL SECTION

4.1 | Material characterization

The morphology of the samples was characterized by scanning electron microscopy (SEM, ZEISS Crossbeam XB340, equipped with an energy dispersive X-ray [EDX] spectrometer, X-treme Oxford instruments), the cross-sectional analysis was conducted using a Capella FIB with gallium ion source. The milling and polishing currents were 30 and 3 nA, respectively, at an acceleration voltage of 30 kV. All samples recovered from cycled cells were transferred to the microscope under argon atmosphere using an air-tight transfer box (SEMILAB). The SEM micrographs were acquired from the top and in cross-sectional configuration after FIB preparation using the smart SEM software for tilt correction to compensate for the image distortion due to the 54° tilt from the optical axis. Powder x-ray diffraction (XRD) patterns were collected employing a Bruker D8 diffractometer, equipped with a Cu-Kα source ($\lambda = 0.15406$ nm) in the 2θ range of $10° < 2\theta < 138°$ with a step size of 0.025° for the powder, and in the 2θ range of $10° < 2\theta < 90°$ with a step size of 0.03° for the electrodes. Rietveld refinement was performed using the GSAS software.[54] A trigonal structure ($R\overline{3}m$, 166) was assumed for all patterns and manually edited to consider a fixed elemental composition of Ni:Co:Mn:B = 83:11:5:1. Two different Wyckoff sites were considered for Ni, that is, the *3b* and *3a* sites, corresponding to the typical transition metal intraplanar layer and the Li octahedral interslab sites, respectively, to account for the transition metal migration to the Li site. The total fraction of Ni was constrained $\left(Ni^{3a} + Ni^{3b} = 0.83\right)$, while atoms in the *3b* sites were considered equivalent. Only Ni was allowed to migrate, given its high fraction in the material and the similar scattering to Co and Mn. The instrumental parameters were obtained from a LaB_6 standard. Accordingly, the instrumental broadening parameters, that is, U, V, W, X, and Y, were kept fixed to $4.397 \times 10^4\,deg^2$, $-5.720 \times 10^4\,deg^2$, $2.577 \times 10^4\,deg^2$, $1.855 \times 10^2\,deg$, and $2 \times 10^5\,deg$, respectively. The peak shape was refined with a generalized microstrain broadening model by optimizing the respective parameters, which were calculated as unitless fraction of $\frac{\Delta d}{d} \times 10^6$ (d being the interplanar distance). The scale, background, sample displacement, unit cell parameters, peak shape, and atomic parameters were refined in this order. The elemental composition and chemical state of the topmost surface layer (sampling depth ~3–5 nm) was investigated by x-ray photoelectron spectroscopy (XPS) using a Specs XPS system with a Phoibos 150 energy analyzer. The measurements were performed using a monochromatic Al-Kα radiation (1486.6 eV), a take-off angle of 45°, and pass energies of 30 and 90 eV at the analyzer for the detail and survey spectra, respectively. To avoid any surface contamination, the samples were prepared in an Ar-filled glovebox and transferred in inert gas atmosphere to the sample load lock of the XPS system. In the case of the samples which were recovered after cycling with the LiBOB electrolyte additive, the spectra were acquired directly after transfer and after removal of the topmost surface layer by Ar^+ ion sputtering (30 min with 0.1 μA and 5 kV, the sputter rate was ~0.1 nm min^{-1}). For the binding energy calibration, the C1s main peak was set to 284.8 eV. Peak fitting was accomplished using the CasaXPS software with Shirley-type backgrounds and Gaussian-Lorentzian peak profiles. The P2s peak contribution to the B1s detail spectra was considered by entering a corresponding feature. The position of the P2s peak was fixed by assuming a constant distance between P2p and P2s peak of 57.5 eV (known from a reference measurement with Li_3PO_4). The intensities were related to

25673165, 0, Downloaded from https://onlinelibrary.wiley.com/doi/10.1002/inf2.12462 by Karlsruher Inst F. Technologie, Wiley Online Library on [03/07/2023]. See the Terms and Conditions (https://onlinelibrary.wiley.com/terms-and-conditions) on Wiley Online Library for rules of use; OA articles are governed by the applicable Creative Commons License

the P2p peak, considering the relative sensitivity factors of the P2p and P2s peaks (also corroborated by the reference measurement).

4.2 | Electrochemical measurements

The positive electrodes were prepared by mixing the active material ($LiNi_{0.83}Co_{0.11}Mn_{0.05}B_{0.01}O_2$), conductive carbon Super C65 (IMERYS), and polyvinylidene difluoride binder (PVdF, Solef 6020, Arkema) in a weight ratio of 92:4:4. The slurry, prepared using *N*-methyl-2-pyrrolidone (NMP; anhydrous, >99.5%; Sigma-Aldrich) as dispersant and solvent, was cast onto battery-grade aluminum foil (12 μm). After drying in a hood inside the dry room overnight, the electrodes were punched into disks with a diameter of 12 mm, vacuum-dried at 120°C for 12 h, and finally pressed at 5 tons cm^{-2}. The average active material mass loading was around 3 mg cm^{-2}. The electrochemical performance was evaluated in coin cells or three-electrode Swagelok®-type cells, which were assembled in an argon-filled glove box (MB200B ECO, MBraun; H_2O and O_2 content lower than 0.1 ppm). Lithium-metal foils were punched into disks served as counter (thickness: 300 μm, diameter: 12 mm) and reference electrodes (thickness: 300 μm, diameter: 10 mm) and glass fiber sheets (Whatman GF/D) as separator, which were soaked with the electrolyte solution (1 M $LiPF_6$ in ethyl carbonate [EC]/dimethyl carbonate [DMC], 1:1 w/w, UBE). Galvanostatic dis-/charge cycling was performed at 20 ± 2°C utilizing a Maccor S4300 battery tester. The applied dis-/charge rate of 1C corresponds to a specific current of 200 mA g^{-1}. All potential/voltage values given herein refer to the Li^+/Li quasi-reference redox couple. The anodic electrochemical stability of the electrolyte with and without the additive was evaluated by linear sweep voltammetry (Solartron 1260) using Pt as the working electrode and Li-metal as the counter electrode. The cell voltage was swept with 0.1 mV s^{-1} from the OCV toward more positive voltages. Electrochemical impedance spectroscopy (EIS) was performed using a VMP multichannel potentiostat from BioLogic. The impedance spectra were collected from the cells in the fully discharged state within the frequency range from 1 MHz to 10 mHz by applying a 5 mV voltage amplitude at 20 ± 2°C.

4.3 | Computational studies

Density functional theory (DFT) calculations were performed with the Vienna ab initio Package (VASP),[55,56] using the Perdew, Burke, and Ernzerhof (PBE)[57] formulation within the generalized gradient approximation (GGA). The projected augmented wave (PAW) potentials[58,59] were chosen to describe the ionic cores and taking valence electrons into account using a plane wave basis set with a kinetic energy cut-off of 450 eV. Partial occupancies of the Kohn–Sham orbitals were allowed using the Gaussian smearing method and a width of 0.05 eV. On-site corrections (DFT + U) were applied to the *3d* electrons of the Ni atoms ($U_{eff} = 6.2$ eV) using the approach from Dudarev et al.[60] The electronic energy was considered self-consistent when the energy change was smaller than 10^{-5} eV. Geometry optimization was considered convergent when the force change was smaller than 0.02 eV $Å^{-1}$. Grimme's DFT-D3 methodology[61] was used to describe the dispersion interactions.

The equilibrium lattice constants of hexagonal $LiNiO_2$ unit cell were optimized using a 15 × 15 × 4 Monkhorst-Pack k-point grid for Brillouin zone sampling to be $a = b = 2.905$ Å and $c = 14.402$ Å. Then a $LiNiO_2$(104) surface model was constructed with $p(4 \times 1)$ periodicity in the *X* and *Y* directions and four stoichiometric layers in the *Z* direction by vacuum depth of 15 Å to separate the surface slab from its periodic duplicates. This model comprises 48 Li, 48 Ni, and 96 O atoms. Eight Ni atoms were replaced by 5 Co and 3 Mn atoms. During the structural optimization, the Γ point in the Brillouin zone was used for *k*-point sampling, and the bottom two stoichiometric layers were fixed while the rest were allowed to fully relax.

The adsorption energy (E_{ads}) of adsorbate *A* was defined as

$$E_{ads} = E_{A/surf} - E_{surf} - E_{A(g)}$$

where $E_{A/surf}$, E_{surf}, and $E_{A(g)}$ are the energy of the adsorbate A adsorbed on the polyimide, the energy of clean polyimide, and the energy of isolated A molecule in a cubic periodic box with a side length of 20 Å and a 1 × 1 × 1 Monkhorst-Pack *k*-point grid for Brillouin zone sampling, respectively.

AUTHOR CONTRIBUTIONS

Fanglin Wu prepared the electrodes, performed the material characterization and electrochemical measurements, and drafted the manuscript. Angelo Mullaliu performed the refinement of the XRD measurements. Thomas Diemant carried out and analyzed the XPS measurements. Dominik Stepien performed the cross-sectional SEM/FIB measurements. Jae-Kwang Kim supplied the NCM83 materials. Dominic Bresser provided funding for the work and supervised Dominik Stepien. Guk-Tae Kim conceptualized the activities and supervised the experimental work. Stefano Passerini conceptualized and coordinated the activities and provided funding for the work. All authors helped to revise the manuscript.

25673165, 0, Downloaded from https://onlinelibrary.wiley.com/doi/10.1002/inf2.12462 by Karlsruher Inst F. Technologie, Wiley Online Library on [03/07/2023]. See the Terms and Conditions (https://onlinelibrary.wiley.com/terms-and-conditions) on Wiley Online Library for rules of use; OA articles are governed by the applicable Creative Commons License

ACKNOWLEDGMENTS

Fanglin Wu gratefully acknowledges the financial support from the Chinese Scholarship Council (CSC). Moreover, the authors would like to acknowledge the financial support from the Helmholtz Association and the European Commission in the frame of the SiGNE project (875557). Jae-Kwang Kim acknowledges the support from the Advancement of Technology (KIAT) and the National Research Foundation of Korea (NRF) grant funded by the Korea Government (P0011933 and 2021R1A4A2001687). Open Access funding enabled and organized by Projekt DEAL.

CONFLICT OF INTEREST STATEMENT

The authors declare no conflict of interest.

ORCID

Stefano Passerini https://orcid.org/0000-0002-6606-5304

REFERENCES

1. Cheng F, Zhang X, Qiu Y, et al. Tailoring electrolyte to enable high-rate and super-stable Ni-rich NCM cathode materials for Li-ion batteries. *Nano Energy*. 2021;88:106301.
2. He M, Su CC, Feng Z, et al. High voltage $LiNi_{0.5}Mn_{0.3}Co_{0.2}O_2$/-graphite cell cycled at 4.6 V with a FEC/HFDEC-based electrolyte. *Adv Energy Mater*. 2017;7(15):1700109.
3. Li W, Erickson EM, Manthiram A. High-nickel layered oxide cathodes for lithium-based automotive batteries. *Nat Energy*. 2020;5(1):26-34.
4. Liu W, Oh P, Liu X, et al. Nickel-rich layered lithium transition-metal oxide for high-energy lithium-ion batteries. *Angew Chem*. 2015;54(15):4440-4457.
5. Yang X, Lin M, Zheng G, et al. Enabling stable high-voltage $LiCoO_2$ operation by using synergetic interfacial modification strategy. *Adv Funct Mater*. 2020;30(43):2004664.
6. Wang Y, Zhang Q, Xue ZC, et al. An in situ formed surface coating layer enabling $LiCoO_2$ with stable 4.6 V high-voltage cycle performances. *Adv Energy Mater*. 2020;10(28):2001413.
7. Song SH, Cho M, Park I, et al. High-voltage-driven surface structuring and electrochemical stabilization of Ni-rich layered cathode materials for Li rechargeable batteries. *Adv Energy Mater*. 2020;10(23):2000521.
8. Li W, Liu X, Xie Q, You Y, Chi M, Manthiram A. Long-term cyclability of NCM-811 at high voltages in lithium-ion batteries: an in-depth diagnostic study. *Chem Mater*. 2020;32(18):7796-7804.
9. Wu F, Kim GT, Kuenzel M, et al. Elucidating the effect of iron doping on the electrochemical performance of cobalt-free lithium-rich layered cathode materials. *Adv Energy Mater*. 2019;9(43):1902445.
10. Zhang L, Ma Y, Cheng X, et al. Enhancement of high voltage cycling performance and thermal stability of $LiNi_{1/3}Co_{1/3}Mn_{1/3}O_2$ cathode by use of boron-based additives. *Solid State Ionics*. 2014;263:146-151.
11. Ji Y, Li S, Zhong G, et al. Synergistic effects of suberonitrile-LiBOB binary additives on the electrochemical performance of high-voltage $LiCoO_2$ electrodes. *J Electrochem Soc*. 2015;162(13):A7015-A7023.
12. Li X, Liu J, Banis MN, et al. Atomic layer deposition of solid-state electrolyte coated cathode materials with superior high-voltage cycling behavior for lithium ion battery application. *Energy Environ Sci*. 2014;7(2):768-778.
13. Jamil S, Ran Q, Yang L, et al. Improved high-voltage performance of $LiNi_{0.87}Co_{0.1}Al_{0.03}O_2$ by Li+-conductor coating. *Chem Eng J*. 2021;407:126442.
14. Zou P, Lin Z, Fan M, Wang F, Liu Y, Xiong X. Facile and efficient fabrication of Li_3PO_4-coated Ni-rich cathode for high-performance lithium-ion battery. *Appl Surf Sci*. 2020;504:144506.
15. Wu F, Fang S, Kuenzel M, et al. Dual-anion ionic liquid electrolyte enables stable Ni-rich cathodes in lithium-metal batteries. *Joule*. 2021;5(8):2177-2194.
16. Xue W, Huang M, Li Y, et al. Ultra-high-voltage Ni-rich layered cathodes in practical Li metal batteries enabled by a sulfonamide-based electrolyte. *Nat Energy*. 2021;6(5):495-505.
17. Zhou L, Zuo TT, Kwok CY, et al. High areal capacity, long cycle life 4 V ceramic all-solid-state Li-ion batteries enabled by chloride solid electrolytes. *Nat Energy*. 2022;7(1):83-93.
18. Ren X, Zou L, Cao X, et al. Enabling high-voltage lithium-metal batteries under practical conditions. *Joule*. 2019;3(7):1662-1676.
19. Deng T, Cao L, He X, et al. In situ formation of polymer-inorganic solid-electrolyte interphase for stable polymeric solid-state lithium-metal batteries. *Chem*. 2021;7(11):3052-3068.
20. Deng T, Fan X, Cao L, et al. Designing in-situ-formed interphases enables highly reversible cobalt-free $LiNiO_2$ cathode for Li-ion and Li-metal batteries. *Joule*. 2019;3(10):2550-2564.
21. Fang S, Wu F, Zarrabeitia M, et al. Enhancing the interfacial stability of high-energy Si/graphite vertical bar vertical bar $LiNi_{0.88}Co_{0.09}Mn_{0.03}O_2$ batteries employing a dual-anion ionic liquid-based electrolyte. *Batteries & Supercaps*. 2022;5(10):e202200286.
22. Chen Y, Zhao W, Zhang Q, et al. Armoring $LiNi_{1/3}Co_{1/3}Mn_{1/3}O_2$ cathode with reliable fluorinated organic–inorganic hybrid interphase layer toward durable high rate battery. *Adv Funct Mater*. 2020;30(19):2000396.
23. Lee Y-M, Nam KM, Hwang EH, et al. Interfacial origin of performance improvement and fade for 4.6 V $LiNi_{0.5}Co_{0.2}Mn_{0.3}O_2$ battery cathodes. *J Phys Chem C*. 2014;118(20):10631-10639.
24. Zhao W, Zheng B, Liu H, et al. Toward a durable solid electrolyte film on the electrodes for Li-ion batteries with high performance. *Nano Energy*. 2019;63:103815.
25. Qian Y, Kang Y, Hu S, et al. Mechanism study of unsaturated tripropargyl phosphate as an efficient electrolyte additive forming multifunctional interphases in lithium ion and lithium metal batteries. *ACS Appl Mater Interfaces*. 2020;12(9):10443-10451.
26. Han JG, Lee SJ, Lee J, Kim JS, Lee KT, Choi NS. Tunable and robust phosphite-derived surface film to protect lithium-rich cathodes in lithium-ion batteries. *ACS Appl Mater Interfaces*. 2015;7(15):8319-8329.

25673165, 0, Downloaded from https://onlinelibrary.wiley.com/doi/10.1002/inf2.12462 by Karlsruher Inst F. Technologie, Wiley Online Library on [03/07/2023]. See the Terms and Conditions (https://onlinelibrary.wiley.com/terms-and-conditions) on Wiley Online Library for rules of use; OA articles are governed by the applicable Creative Commons License

27. Kazzazi A, Bresser D, Kuenzel M, et al. Synergistic electrolyte additives for enhancing the performance of high-voltage lithium-ion cathodes in half-cells and full-cells. *J Power Sources*. 2021;482:228975.
28. Mao M, Huang B, Li Q, Wang C, He Y-B, Kang F. In-situ construction of hierarchical cathode electrolyte interphase for high performance $LiNi_{0.8}Co_{0.1}Mn_{0.1}O_2$/Li metal battery. *Nano Energy*. 2020;78:105282.
29. Dalavi S, Xu M, Knight B, Lucht BL. Effect of added LiBOB on high voltage ($LiNi_{0.5}Mn_{1.5}O_4$) spinel cathodes. *Electrochem Solid-State Lett*. 2011;15(2):A28-A31.
30. Xu M, Zhou L, Dong Y, Chen Y, Garsuch A, Lucht BL. Improving the performance of graphite/ $LiNi_{0.5}Mn_{1.5}O_4$ cells at high voltage and elevated temperature with added lithium bis(oxalato) borate (LiBOB). *J Electrochem Soc*. 2013;160(11): A2005-A2013.
31. Zhu Y, Li Y, Bettge M, Abraham DP. Electrolyte additive combinations that enhance performance of high-capacity $Li_{1.2}Ni_{0.15}Mn_{0.55}Co_{0.1}O_2$–graphite cells. *Electrochim Acta*. 2013; 110:191-199.
32. Xiao Z, Liu J, Fan G, et al. Lithium bis (oxalate) borate additive in the electrolyte to improve Li-rich layered oxide cathode materials. *Mater Chem Front*. 2020;4(6):1689-1696.
33. Li Y, Li W, Shimizu R, et al. Elucidating the effect of borate additive in high-voltage electrolyte for Li-rich layered oxide materials. *Adv Energy Mater*. 2022;12(11):2103033.
34. Xu C, Reeves PJ, Jacquet Q, Grey CP. Phase behavior during electrochemical cycling of Ni-rich cathode materials for Li-ion batteries. *Adv Energy Mater*. 2020;11(7):2003404.
35. Zheng J, Yan P, Estevez L, Wang C, Zhang J-G. Effect of calcination temperature on the electrochemical properties of nickel-rich $LiNi_{0.76}Mn_{0.14}Co_{0.10}O_2$ cathodes for lithium-ion batteries. *Nano Energy*. 2018;49:538-548.
36. Kim U-H, Kuo L-Y, Kaghazchi P, Yoon CS, Sun Y-K. Quaternary layered Ni-rich NCMA cathode for lithium-ion batteries. *ACS Energy Lett*. 2019;4(2):576-582.
37. Oh P, Ko M, Myeong S, Kim Y, Cho J. A novel surface treatment method and new insight into discharge voltage deterioration for high-performance $0.4Li_2MnO_{3-0.6}LiNi_{1/3}Co_{1/3}Mn_{1/3}O_2$ cathode materials. *Adv Energy Mater*. 2014;4(16):1400631.
38. Wang X, Ding YL, Deng YP, Chen Z. Ni-rich/Co-poor layered cathode for automotive Li-ion batteries: promises and challenges. *Adv Energy Mater*. 2020;12:1903864.
39. Heist A, Hafner S, Lee S-H. High-energy nickel-rich layered cathode stabilized by ionic liquid electrolyte. *J Electrochem Soc*. 2019;166(6):A873-A879.
40. Yan P, Zheng J, Liu J, et al. Tailoring grain boundary structures and chemistry of Ni-rich layered cathodes for enhanced cycle stability of lithium-ion batteries. *Nat Energy*. 2018;3(7): 600-605.
41. Cheng X, Liu M, Yin J, et al. Regulating surface and grain-boundary structures of Ni-rich layered cathodes for ultrahigh cycle stability. *Small*. 2020;16(13):e1906433.
42. Bai P, Ji X, Zhang J, et al. Formation of LiF-rich cathode-electrolyte interphase by electrolyte reduction. *Angew Chem Int Ed*. 2022;61(26):e202202731.
43. Zhao W, Zheng J, Zou L, et al. High voltage operation of Ni-rich NMC cathodes enabled by stable electrode/electrolyte interphases. *Adv Energy Mater*. 2018;8(19):1800297.
44. Peng H-J. Unravelling the cell ageing phenomena in aprotic lithium-nickel-cobalt-manganese-oxide batteries.(Doctoral thesis). ETH Zürich, Zürich, Switzerland. 2016.
45. Hong M, Lee S, Ho V-C, Lee D, Yu S-H, Mun J. Unraveling the dynamic interfacial behavior of $LiCoO_2$ at various voltages with lithium Bis(oxalato)borate for lithium-ion batteries. *ACS Appl Mater Interfaces*. 2022;14(8):10267-10276.
46. Lu W, Chen Z, Joachin H, Prakash J, Liu J, Amine K. Thermal and electrochemical characterization of MCMB/$LiNi_{1/3}Co_{1/3}Mn_{1/3}O_2$ using LiBoB as an electrolyte additive. *J Power Sources*. 2007;163(2):1074-1079.
47. Saruwatari H, Kuboki T, Kishi T, Mikoshiba S, Takami N. Imidazolium ionic liquids containing LiBOB electrolyte for lithium battery. *J Power Sources*. 2010;195(5):1495-1499.
48. Kim J-H, Kim SJ, Yuk T, Kim J, Yoon CS, Sun Y-K. Variation of electronic conductivity within secondary particles revealing a capacity-fading mechanism of layered Ni-rich cathode. *ACS Energy Lett*. 2018;3(12):3002-3007.
49. Li T, Yuan X-Z, Zhang L, Song D, Shi K, Bock C. Degradation mechanisms and mitigation strategies of nickel-rich NMC-based lithium-ion batteries. *Electrochem Energy Rev*. 2019; 3(1):43-80.
50. Storch M, Fath JP, Sieg J, et al. Cycle parameter dependent degradation analysis in automotive lithium-ion cells. *J Power Sources*. 2021;506:230227.
51. de Biasi L, Schiele A, Roca-Ayats M, et al. Phase transformation behavior and stability of $LiNiO_2$ cathode material for Li-ion batteries obtained from in situ gas analysis and operando X-ray diffraction. *ChemSusChem*. 2019;12(10): 2240-2250.
52. Ryu H-H, Park G-T, Yoon CS, Sun Y-K. Suppressing detrimental phase transitions via tungsten doping of $LiNiO_2$ cathode for next-generation lithium-ion batteries. *J Mater Chem A*. 2019; 7(31):18580-18588.
53. Wen S, Han Y, Wang P, et al. An interfacial mechanism of chelate-borate electrolyte additives in Ni-rich $LiNi_{0.8}Mn_{0.1}Co_{0.1}O_2$ cathodes. *ACS Appl Energy Mater*. 2021;4(11):12525-12534.
54. Toby BH, Von Dreele RB. GSAS-II: the genesis of a modern open-source all purpose crystallography software package. *J Appl Crystallogr*. 2013;46(2):544-549.
55. Kresse G, Furthmüller J. Efficient iterative schemes for ab initio total-energy calculations using a plane-wave basis set. *Phys Rev B*. 1996;54(16):11169-11186.
56. Kresse G, Furthmüller J. Efficiency of ab-initio total energy calculations for metals and semiconductors using a plane-wave basis set. *Comput Mater Sci*. 1996;6(1):15-50.
57. Perdew JP, Burke K, Ernzerhof M. Generalized gradient approximation made simple. *Phys Rev Lett*. 1996;77(18):3865-3868.
58. Kresse G, Joubert D. From ultrasoft pseudopotentials to the projector augmented-wave method. *Phys Rev B*. 1999;59(3): 1758-1775.
59. Blöchl PE. Projector augmented-wave method. *Phys Rev B*. 1994;50(24):17953-17979.
60. Dudarev SL, Botton GA, Savrasov SY, Humphreys CJ, Sutton AP. Electron-energy-loss spectra and the structural stability of nickel oxide: an LSDA+U study. *Phys Rev B*. 1998; 57(3):1505-1509.
61. Grimme S, Antony J, Ehrlich S, Krieg H. A consistent and accurate ab initio parametrization of density functional

25673165, 0, Downloaded from https://onlinelibrary.wiley.com/doi/10.1002/inf2.12462 by Karlsruher Inst F. Technologie, Wiley Online Library on [03/07/2023]. See the Terms and Conditions (https://onlinelibrary.wiley.com/terms-and-conditions) on Wiley Online Library for rules of use; OA articles are governed by the applicable Creative Commons License

dispersion correction (DFT-D) for the 94 elements H-Pu. *J Chem Phys*. 2010;132(15):154104.

SUPPORTING INFORMATION

Additional supporting information can be found online in the Supporting Information section at the end of this article.

How to cite this article: Wu F, Mullaliu A, Diemant T, et al. Beneficial impact of lithium bis (oxalato)borate as electrolyte additive for high-voltage nickel-rich lithium-battery cathodes. *InfoMat*. 2023;e12462. doi:10.1002/inf2.12462

25673165, 0, Downloaded from https://onlinelibrary.wiley.com/doi/10.1002/inf2.12462 by Karlsruher Inst F. Technologie, Wiley Online Library on [03/07/2023]. See the Terms and Conditions (https://onlinelibrary.wiley.com/terms-and-conditions) on Wiley Online Library for rules of use; OA articles are governed by the applicable Creative Commons License